

Running Head

Cell Wall Architecture in *Zinnia elegans* Tracheary Elements

Corresponding Author

Michael P. Thelen

Physical and Life Sciences Directorate

Lawrence Livermore National Laboratory, L-452

PO Box 808

Livermore, CA 94550

Office: (925) 422-6547

Fax: (925) 422-2282

Email: mthelen@llnl.gov

Journal Research Area

Cell Biology

Imaging Cell Wall Architecture in Single *Zinnia elegans* Tracheary Elements*

Catherine I. Lacayo¹, Alexander J. Malkin¹, Hoi-Ying N. Holman², Liang Chen², Shi-You Ding^{3,4}, Mona S. Hwang¹, and Michael P. Thelen^{1,5, §}

¹Physical & Life Sciences Directorate, Lawrence Livermore National Laboratory, Livermore, CA;

²Earth Sciences Division, Lawrence Berkeley National Laboratory, Berkeley, CA;

³Biosciences Center, National Renewable Laboratory, Golden, CO;

⁴BioEnergy Science Center, Oak Ridge National Laboratory, Oak Ridge, TN;

⁵Joint BioEnergy Institute, Emeryville, CA

Footnotes

* This research was funded by the U.S. Department of Energy Genome Sciences Program. MPT was funded by the Office of Biological and Environmental Research (OBER) Grant SCW0738 and by the DOE Joint BioEnergy Institute (JBEI). Work at Lawrence Livermore National Laboratory was carried out under the auspices of the DOE under Contract DE-AC52-07NA27344. H-YNH was supported by the OBER Biological Systems Science Division, Biofuels Science Focus Area, through contracts DE-AC02-05CH11231 and KP1501021 with Lawrence Berkeley National Laboratory. S-YD was funded by the BioEnergy Science Center (BESC) and OBER.

Institution paper number, LLNL-JRNL-424083

§ Correspondence to MPT: mthelen@llnl.gov

ABSTRACT

The chemical and structural organization of the plant cell wall was examined in *Zinnia elegans* tracheary elements (TEs), which specialize by developing prominent secondary wall thickenings underlying the primary wall during xylogenesis *in vitro*. Three imaging platforms were used in conjunction with chemical extraction of wall components to investigate the composition and structure of single *Zinnia* TEs. Using fluorescence microscopy with a GFP-tagged *Clostridium thermocellum* family 3 carbohydrate-binding module specific for crystalline cellulose, we found that cellulose accessibility and binding in TEs increased significantly following an acidified chlorite treatment. Examination of chemical composition by synchrotron radiation-based Fourier-transform infrared spectromicroscopy indicated a loss of lignin and a modest loss of other polysaccharides in treated TEs. Atomic force microscopy (AFM) was used to extensively characterize the topography of cell wall surfaces in TEs, revealing an outer granular matrix covering the underlying meshwork of cellulose fibrils. The internal organization of TEs was determined using secondary wall fragments generated by sonication. AFM revealed that the resulting rings, spirals and reticulate structures were composed of fibrils arranged in parallel. Based on these combined results, we generated an architectural model of *Zinnia* TEs comprised of three layers: an outermost granular layer, a middle primary wall composed of a meshwork of cellulose fibrils, and inner secondary wall thickenings containing parallel cellulose fibrils. In addition to insights in plant biology, studies using *Zinnia* TEs could prove especially productive in assessing cell wall responses to enzymatic and microbial degradation, thus aiding current efforts in lignocellulosic biofuel production.

INTRODUCTION

The organization and molecular architecture of plant cell walls represent some of the most challenging problems in plant biology. Although much is known about general aspects of assembly and biosynthesis of the plant cell wall, the detailed three-dimensional molecular cell wall structure remains poorly understood. The highly complex and dynamic nature of the plant cell wall has perhaps limited the generation of such detailed structural models. This information is pivotal for the successful implementation of novel approaches for conversion of biomass to liquid biofuels given that one of the critical processing steps in biomass conversion involves systematic deconstruction of cell walls. Therefore, a comprehensive understanding of the architecture and chemical composition of the plant cell wall will not only help develop molecular-scale models, but will also help improve the efficiency of biomass deconstruction.

The composition and molecular organization of the cell wall is species and cell type dependent (Vorwerk et al., 2004). Thus, the development of a model plant system, which utilizes a single cell type, has enhanced our capacity to understand cell wall architecture. The ability to generate a population of single *Zinnia elegans* plant cells that were synchronized throughout cell wall deposition during xylogenesis was developed in the 1980s (Fukuda and Komamine, 1980). Mesophyll cells isolated from the leaves of *Zinnia* and cultured in the presence of phytohormones will transdifferentiate into tracheary elements (TEs), which are individual components of the xylem vascular tissue (Fukuda and Komamine, 1980). During this transdifferentiation process, TEs gradually develop patterned secondary wall thickenings, commonly achieving annular, spiral, reticulate, scalariform, or pitted patterns (Bierhorst, 1960; Falconer and Seagull, 1988; Roberts and Haigler, 1994). These secondary wall thickenings serve as structural reinforcements that add strength and rigidity to prevent the collapse of the xylem under the high pressure created by fluid transport. During the final stages of transdifferentiation, TEs accumulate lignin in their secondary walls and undergo programmed cell death, which results in the removal of all cell contents leaving behind a “functional corpse” (Roberts and McCann, 2000; Fukuda, 2004).

In broad terms, the primary cell wall of higher plants is mainly composed of three types of polysaccharides: cellulose, hemicelluloses and pectins (Cosgrove, 2005). Cellulose is composed

of unbranched β -1,4-glucose chains that are packed together into fibrils by inter- and intramolecular hydrogen bonding. Hemicelluloses and pectins are groups of complex polysaccharides, which are primarily comprised of xyloglucans/xylans and galacturonans, respectively. Hemicelluloses are involved in cross-linking and associating with cellulose microfibrils, while pectins control wall porosity and help bind neighboring cells together. The patterned deposits of secondary wall in *Zinnia* TEs primarily consist of cellulose microfibrils, along with hemicelluloses, and also lignin, a complex aromatic polymer that is characteristic of secondary walls and provides reinforcement (Turner et al., 2007). All the molecular components in the cell wall correspond to a multitude of different polysaccharides, phenolic compounds, and proteins that become arranged and modified *in muro*, yielding a structure of great strength and resistance to degradation.

Currently, electron microscopy (EM) is the primary tool for structural studies of cell walls and has provided remarkable information regarding wall organization. Fast-freeze deep-etch EM in combination with chemical and enzymatic approaches, have generated recent models of the architecture of the primary wall (McCann et al., 1990; Carpita and Gibeaut, 1993; Nakashima et al., 1997; Fujino et al., 2000; Somerville et al., 2004). Direct visualization of secondary wall organization has been focused towards the examination of multiple wall layers in wood cells (Fahlen and Salmen, 2005; Zimmermann et al., 2006). However, few studies have examined the secondary wall, so our knowledge regarding the higher order architecture of this type of wall is limited. Over the past few decades, atomic force microscopy (AFM) has provided new opportunities to probe biological systems with spatial resolution similar to EM techniques (Kuznetsov et al., 1997; Muller et al., 1999), with additional ease of sample preparation and the capability to probe living native structures. Over the past decades, AFM has been successfully applied to studies of the high-resolution architecture, assembly and structural dynamics of a wide range of biological systems (Hoh et al., 1991; Crawford et al., 2001; Malkin et al., 2003; Plomp et al., 2007), thus enabling the observation of the ultrastructure of the plant cell wall, which is of particular interest to us (Kirby et al., 1996; Morris et al., 1997; Davies and Harris, 2003; Yan et al., 2004; Ding and Himmel, 2006).

To generate more detailed structural models, knowledge about the structural organization of the cell wall can be combined with spatial information about chemical composition. Instead of

utilizing chromatography techniques to analyze cell wall composition by extracting material from bulk plant samples (Mellerowicz et al., 2001; Pauly and Keegstra, 2008), Fourier transform infrared (FTIR) spectromicroscopy can be used to directly probe for polysaccharide and aromatic molecules in native as well as treated plant material (Carpita et al., 2001; McCann et al., 2001). FTIR spectromicroscopy is not only able to identify the chemical components in a specific system, but also determine their distribution and relative abundance. This technique also improves the sensitivity and spatial resolution of cellular components without the derivatization needed by chemical analysis using chromatography. Polysaccharide specific probes, such as carbohydrate-binding modules (CBMs), can also be used to understand the chemical composition of the plant cell wall. CBMs are non-catalytic protein domains existing in many glycoside hydrolases. Based on their binding specificities, CBMs are generally categorized into three groups: surface-binding CBMs specific for insoluble cellulose surfaces, chain-binding CBMs specific for single chains of polysaccharides, and end-binding CBMs specific for the ends of polysaccharides or oligosaccharides. A surface-binding CBM with high affinity for the planar faces of crystalline cellulose (Tormo et al., 1996; Lehtio et al., 2003) has been fluorescently labeled and used to label crystals as well as plant tissue (Ding et al., 2006; Porter et al., 2007; Liu et al., 2009; Xu et al., 2009). The binding capacity of the CBM family has been further exploited for the detection of different polysaccharides, such as xylans and glucans, and can thus be used for the characterization of plant cell wall composition (McCartney et al., 2004; McCartney et al., 2006).

In the present study, we used a combination of AFM, synchrotron radiation-based FTIR spectromicroscopy, and fluorescence microscopy using a cellulose-specific CBM to probe the cell wall of *Zinnia* TEs. The *Zinnia* TE culture system proved ideal for observing the structure and chemical composition of the cell wall because it comprises a single homogeneous cell type, representing a simpler system compared to plant tissues, which may contain multiple cell types. *Zinnia* TEs were also advantageous because they were analyzed individually and population statistics were generated based on specific conditions or treatments. Furthermore, cultured *Zinnia* TEs were used for the consistent production of cell wall fragments for analysis of the organization of internal secondary wall structures. In summary, we have physically and

chemically dissected *Zinnia* TEs using a combination of imaging techniques that revealed primary and secondary wall structure and enabled reconstruction of TE cell wall architecture.

RESULTS

Cultured Tracheary Elements can be Separated from Mesophyll Cells

When mesophyll cells from the leaves of *Zinnia* were induced to differentiate into tracheary elements (TEs), we observed a modest percentage (approximately 20 to 40%) of TEs develop after 4 days or longer in culture. Since the primary goal of this study was focused on examining the organization and chemical composition of the primary wall and the secondary wall thickenings of TEs, we developed a method to separate and enrich TEs. We took advantage of the substantial physical differences between mesophyll cells, dead cells, and TEs to separate them by density gradient centrifugation. After fractionation of *Zinnia* cultures, three bands were evident: a top green band, which primarily contained mesophyll and dead cells, a middle more diffuse band, which contained a mixture of mesophyll cells and TEs, and a lower dense band, which was observed to be highly enriched in TEs and contain up to 95% TEs (Fig. 1A, B). This separation method enhanced our ability to detect TEs by SR-FTIR and AFM compared to crude cell cultures that contained undifferentiated and dead cells in addition to TEs. Light microscopy and AFM revealed that the overall integrity, morphology, and topography of fractionated TEs were not affected compared to non-fractionated cultured cells. Chloroplasts were clearly apparent in mesophyll cells (Fig. 1C, D); while TEs exhibited prominent secondary wall thickenings arranged in spiral patterns or more complex reticulate shapes that were highly autofluorescent (Fig. 1A, inset). TEs were particularly discernible from mesophyll cells by the detection of secondary cell wall thickenings (Fig. 1E, F).

Oxidative Treatment Enhances CtCMB3 Labeling of Single Tracheary Elements

To complement these gross morphological observations of TEs, we probed *Zinnia* TEs for the presence of crystalline cellulose. For this purpose, we used a GFP-tagged family 3 CBM derived from the scaffoldin protein of *Clostridium thermocellum* cellulosome (CtCBM3) to specifically

detect cellulose (Ding et al., 2006; Xu et al., 2009). To determine if the presence of lignin affected CBM3 binding to the cell wall, we performed an oxidative treatment (1% sodium chlorite, 0.14% acetic acid at 70°C) that has been traditionally used to delignify wood samples (Leavitt and Danzer, 1993). Lignin removal from *Zinnia* TEs treated with acidified chlorite was qualitatively confirmed by phloroglucinol staining (not shown). To account for cell-to-cell variability, we also quantified the fluorescence of TEs and performed population analysis. We observed that the autofluorescence of the secondary wall thickenings of TEs treated with acidified chlorite was lost and equivalent to background levels (Fig. 2C, E). These TEs also appeared much thinner and less rigid (Fig. 2C, D). When TEs incubated in water at 70°C (control) were labeled with *Ct*CBM3-GFP, the fluorescence was greater than in unlabeled TEs (Fig. 2A, B and E). This result, which was similar for TEs that were incubated in water at room temperature (not shown), suggested that *Ct*CBM3-GFP was binding to accessible cellulose in the cell wall. Similarly, *Ct*CBM3-GFP labeling significantly increased the fluorescence of TEs that were treated in oxidative conditions (Fig 2C, D, E, $p < 0.0001$). More interestingly, the fluorescence of these treated TEs labeled with *Ct*CBM3-GFP was significantly increased compared to all other TE populations (Fig. 2E, $p < 0.0001$). The average total fluorescence of these *Ct*CBM3-GFP-labeled treated TEs was roughly 4 times greater than for labeled control TEs, 20 times greater than for unlabeled control TEs, and 1000 times greater than for unlabeled treated TEs (Fig. 2E). These observations demonstrate that oxidative treatment with acidified chlorite improved the accessibility and binding of the *Ct*CBM3-GFP probe and that most binding was to cellulose in the secondary wall.

Primary Wall Microfibrils Form a Meshwork Coated by a Granular Matrix

Since we had observed changes in cellulose accessibility after acidified chlorite treatment, we decided to closely examine *Zinnia* TEs following this treatment using AFM to obtain high-resolution topographical information. We found that initially, without any oxidative treatment, air-dried TEs were covered by granular material on the outermost surface (Fig. 3A, B). These granules appeared to vary in size ranging from 20 to 50 nm (Fig. 3B) and were observed in TEs that were incubated in water at room temperature or at 70°C. This granular matrix was also present in fully hydrated TEs imaged in water by AFM and in TEs from both crude and density-separated preparations (not shown).

Oxidative treatment with acidified chlorite at 70°C removed the granular material in most TEs and exposed the meshwork of cellulose fibrils from the primary wall (Fig 3C, D). This result confirmed that the enhanced CBM3-labeling of TEs following a treatment with acidified chlorite (see Fig. 2) was due to the increased exposure of cellulose fibrils. Upon closer examination of the cell wall network, we observed that cellulose fibrils forming this meshwork, lacked any preferential orientation, and could become buried within the meshwork (Fig. 3C, D). Microfibrils were at least 2 μm in length, ranging in width from approximately 8 to 15 nm and, in some cases, appeared to be bundles of smaller fibrils.

Following acidified chlorite treatment, most TEs were completely devoid of the outermost granular material, while a few TEs were observed with granular regions remaining (Fig. 3E, F). In some cases, patches of cellulose fibrils were observed through openings in the granular matrix still present on the surface of TEs (Fig. 3E). This observation confirmed that the granular matrix observed on the surface of TEs (Fig. 3A, B) formed a layer encasing the cell wall (Fig. 3E). Any remaining layer of granules was found to be relatively thin and uneven, ranging in thickness from approximately 50 to 200 nm depending on the location of the measurement (Fig. 3E). In other cases, clumps of granules that appeared embedded within cellulose fibrils were observed as remnants of the granular matrix (Fig. 3F).

SR-FTIR Spectromicroscopy Detects Changes in Chemical Composition

To characterize the chemical changes that accompany oxidative treatment of TEs, we used SR-FTIR to measure the absorption of mid infrared light in individual TEs. Since the absorption at particular infrared light frequencies corresponds to specific chemical bonds and groups, we could analyze the major groups composing the cell wall: cellulose, hemicellulose, pectin and lignin. Absorbance spectra were collected by scanning the area of individual hydrated TEs in transmission mode, such that the infrared beam passed through the TEs. Our aim was to generate average chemical information from a group of individual TEs to determine how the composition of TEs changed after treatment with acidified chlorite.

TEs incubated in water at 70°C appeared to lose material with infrared absorbances at $\sim 1738\text{ cm}^{-1}$ and $\sim 1040\text{ cm}^{-1}$ (Fig. 4B). Absorbance at $\sim 1738\text{ cm}^{-1}$ can be attributed to hemicelluloses

and/or pectins, while absorbance at $\sim 1040\text{ cm}^{-1}$ largely correspond to hemicellulose and cellulose from the cell wall. However, this incubation in hot water did not appear to reduce the infrared absorbance intensity at $\sim 1510\text{ cm}^{-1}$, which corresponds to the aromatic groups in lignin (Fig. 4B). TEs incubated in acidified chlorite exhibited a more dramatic change in composition. In addition to a reduction in hemicellulose and pectic materials, the aromatic lignin absorbance signal at $\sim 1510\text{ cm}^{-1}$ was reduced from ~ 0.16 to ~ 0.03 , suggesting a loss of about 80% of the lignin in the treated TEs (Fig. 4C, D). A slight reduction in absorbance was also detected at $\sim 2930\text{ cm}^{-1}$, which corresponds to carbon-hydrogen bonds, suggesting that TEs lose general cell wall components after incubation in hot acidified chlorite. We also performed Principal Component Analysis and Linear Discriminant Analysis (PCA-LDA) to evaluate the statistical significance of the spectral differences among the three different conditions examined. The spectral signatures, and thereby, the composition of TEs treated with acidified chlorite at 70°C are distinctly different from TEs incubated in water at 25°C or 70°C as revealed by PC scores along the first two modes of variation (Fig. 4E).

Tracheary Element Fragments Reveal Parallel Networks of Cellulose Fibrils Forming the Secondary Wall

We had been able to examine the composition of intact *Zinnia* TEs and directly probe the organization of their outermost layer and primary wall. However, we were also interested in probing internal components of the cell wall, in particular, the secondary wall, which is unmistakably observed as cell wall thickenings. Since these secondary wall thickenings are located underneath the primary wall and are thus inaccessible to AFM imaging, we used mild sonication to physically dissect TEs. This approach allowed us to generate TE fragments, which exposed the interior surfaces of the cell wall, and were thus conducive to AFM imaging.

Sonication generated a variety of TE fragments that primarily included substructures from the secondary wall thickenings such as discrete ring-like structures and spiral or reticulate networks (Fig. 5A to C). Rings were particularly interesting because, as shown in Fig. 5D, they could be oriented so that they present a transverse cross-section of a TE. The average diameter of these rings was on average $16.1\text{ }\mu\text{m}$ ($\text{SD}=2.5$, $n=35$), which corresponds well to the diameter of TEs. The central structure of the ring in Fig. 5D corresponded to a secondary wall thickening of

approximately 3 μm in thickness (equivalent to TE depth) and was composed mainly of cellulose fibrils, which were predominantly arranged in parallel, oriented concentrically within the ring. Some of the fibers observed within these thickenings may correspond to other polysaccharides abundant in the wall, such as hemicelluloses. Granules of approximately 20 to 50 nm were also seen within the secondary wall ring. A few individual fibers were observed to run across the main orientation of the parallel fibrils (Fig. 5D, regions 4 and 5). Some regions of the ring appeared to contain more granular material than others (compare region 3 to region 4, for example), but the overall parallel organization of the cellulose fibrils was still evident. A granular layer similar to that previously seen on the surface of TEs (see Fig. 2A, B) was found to surround the central secondary wall ring structure and have an approximate thickness ranging from approximately 0.9 to 2 μm . We could not clearly detect the primary wall, suggesting that it had been essentially degraded or that it was fully covered with granular matrix.

When we examined TE fragments that had been incubated in oxidative conditions, we found that the granular matrix was removed from the secondary wall thickenings. Thus, the parallel cellulose fibrils were devoid of granular particles with a few fibers running transversely (Fig. 5E). In these chemically treated samples, the main orientation of these cellulose fibrils was apparent, revealing that they were positioned parallel to the length of the thickenings. In the case of reticulate networks, fibrils maintained their parallel arrangement, but large groups became reorganized at intersecting points (Fig. 5F). In addition, we observed thicker cellulose bundles of about 30 to 50 nm in width that formed thicker structures of up to 100 nm in width (Fig. 5F).

DISCUSSION

The *Zinnia elegans* mesophyll system of transdifferentiation into TEs has traditionally been used as tool to study xylogenesis *in vitro*, providing important clues about signal-transduction, gene-expression pathways, and molecular mechanisms involved in this process (Fukuda, 2004). Instead of using *Zinnia* TEs to study plant vascularization, we used this system to directly probe both the primary and secondary wall in order to improve our knowledge of TE wall organization and composition. In addition, we analyzed the fluorescence of single cells and generated

quantitative data to distinguish between populations of TEs that were chemically treated and labeled with fluorescent probes.

In vitro differentiation of mesophyll cells into TEs has been shown to occur at remarkably efficient rates (50 to 76%) (Roberts et al., 1992; Roberts and Haigler, 1994; Milioni et al., 2001; Benova-Kakosova et al., 2006; Twumasi et al., 2009); however, lower percentages of differentiated TEs have been also reported (Fukuda and Komamine, 1980; Thelen and Northcote, 1989). In this study, on average, approximately 30% of TEs were observed in our cultures. Variability in TE differentiation could be caused by technical differences, due to variations in the environment in which *Zinnia* plants were cultivated. Therefore, to facilitate the physical and chemical analysis of the cell wall, we developed a density gradient separation method to generate enriched fractions of TEs and facilitate detection by fluorescence microscopy, SR-FTIR spectromicroscopy and AFM. Flow cytometry has been also utilized as a method to separate TEs from mesophyll cells (Ito et al., 2004), but this approach involved the use of exogenous fluorescent labels that could affect cells. An additional report showed that TEs comprise a distinct population based on size and granularity information obtained from light scatter information during flow cytometry (Weir et al., 2005); therefore, isolation of TEs from mesophyll cells could be possible using this method. Nonetheless, the relatively simple density-based approach developed in this report provides means to isolate TEs from mesophyll and dead cells without affecting the overall morphology or detailed surface topography of TEs.

Most of the understanding of the ultrastructure of plant tissue has been obtained using electron microscopy. In this study we employed AFM, which has become a valuable tool to examine cell wall organization in recent years and can provide information complementary to that obtained from electron microscopy. AFM is capable of revealing high resolution structural details from living cells in real time, as demonstrated in bacteria, for example in studies examining spore germination (Plomp et al., 2007) and cell growth and division (Touhami et al., 2004). Recent reviews have highlighted the type of high-resolution dynamic structural information that can be obtained from live bacteria using this technique in fluid (Dufrene, 2008b; Scheuring and Dufrene, 2010). However, in this study we air-dried TEs because of the specific challenges presented by AFM imaging of native single cells in an aqueous environment. The small contact area between a cell and substrate can result in the detachment of cells during imaging, due to

interactions between the AFM cantilever and specimen (Dufrene, 2008a; Fantner et al., 2010). The relatively large size of single *Zinnia* TEs, in addition to their hollow nature, makes surface immobilization difficult and AFM imaging problematic. Recent advances in high-speed AFM (Viani et al., 2000; Kodera et al., 2006), which considerably decrease cantilever-cell interactions (Fantner et al., 2010), may provide future improvements for imaging of cellular dynamics in TEs. Our AFM imaging observations of cellulose fibril organization in air-dried TEs agree with previous reports of microfibril architecture in the cell wall of *Zinnia* TEs using cryo-electron microscopy (Nakashima et al., 1997). Therefore, dehydration of our single cell samples did not appear to have a dramatic effect on the organization of the cell wall of TEs, especially in the inner secondary wall, perhaps due to the presence of matrix materials between microfibrils. Further studies of dehydrated plant material are specifically relevant because of the need for developing biomass treatment strategies, given that biomass for biofuel production is generally dried.

To the best of our knowledge, this is the first study in which AFM has been used to examine the cell wall of TEs, particularly the structure of the inner secondary wall. Our AFM studies provided novel high-resolution structural data, which could be used for the development of more comprehensive three-dimensional TE models. As a result of chemical and physical perturbations that provided access to inner components of *Zinnia* TEs, we were able to reconstruct the high-resolution architecture of different layers in the cell wall: (1) an outermost granular matrix enveloping the TE, (2) the primary wall of cellulose microfibrils organized in a meshwork, and (3) the inner secondary wall thickenings containing mainly cellulose microfibrils arranged in a parallel orientation (see Fig. 6). Cellulose fibrils from these different layers of the wall were embedded within granules, which were omitted from Fig. 6 for presentation purposes. The dimensions of the different parts of TEs, derived from our AFM analysis, were consistent with those previously observed by transmission electron microscopy (Burgess and Linstead, 1984; Taylor et al., 1992; Nakashima et al., 1997; Salnikov et al., 2001; Karlsson et al., 2005). We found that cellulose microfibrils from the primary wall were organized in a meshwork, with fibrils running in multiple directions, while they were mostly arranged in parallel in the secondary wall. As mentioned before, this organization agreed with previously reported observations of cellulose microfibrils in the cell wall of *Zinnia* TEs using freeze-etch replica techniques (Nakashima et al., 1997). The width of cellulose fibrils forming the primary and

secondary walls of *Zinnia* TEs also corresponded to data reported for various plants and techniques used for visualization (Roland et al., 1975; Chanzy et al., 1979; McCann et al., 1990; Fujino et al., 2000; Thimm et al., 2000).

The presence of granular materials in different locations of the cell wall, including the outside surface and secondary cell wall thickenings, was of particular interest. Granules similar to those we found covering *Zinnia* TEs have been previously observed on parenchyma cells from maize (Ding and Himmel, 2006). This material may correspond to pectic substances, which are abundantly present in the middle lamellar surfaces of xylem cells and the surface of single TEs in culture (Burgess and Linstead, 1984; Stacey et al., 1995). Nonetheless, it is important to consider that cultured *Zinnia* TEs develop in an “artificial” environment as single cells rather than in contact with neighboring cells, so their outermost surfaces may not be representative of structures in living plants. In the secondary wall, we observed that the loss of lignin by SR-FTIR correlated well with the absence of granules from chemically treated secondary wall fragments. In addition, other cell wall polymers present in the wall may have possessed lignin deposits that rendered them insoluble, thus removing them along with lignin during oxidative treatment. Therefore, we infer that the granules within the secondary wall thickenings primarily corresponded to lignin. Lignin is known to be a major component of these thickenings in xylem cells (Fukuda and Komamine, 1982; Barceló, 1995) and has been shown to display globular shapes in wood pulp samples (Simola et al., 2000; Poggi et al., 2005). Electron microscopy also has revealed the accumulation of spherical structures, similar to the ones we observed, in the secondary wall of *Zinnia* TEs (Nakashima et al., 1997). Accumulation of these spherical structures was reported to correlate strongly with measurements of UV absorption by lignin (Nakashima et al., 1997). We did not observe any clear crosslinks connecting cellulose fibrils (McCann et al., 1990; Nakashima et al., 1997; Yan et al., 2004), possibly because they were obscured by granules in native TEs or because the hot oxidative treatment used removed hemicellulosic structures in treated TEs (Green, 1963; Leavitt and Danzer, 1993). It is also possible that these crosslinks may not be clearly seen due to the prevalence of the abovementioned granular materials in the wall of TEs.

Physical dissection of TEs through sonication provided direct access to the organization of the internal secondary wall. The presence of ring-like and reticulate network structures in sonicated

samples demonstrated that the breakage of TEs often occurs along secondary wall thickenings. This observation indicated that thickenings represent points of higher mechanical rigidity within TEs. Such fragments appear to be ideally suited for future *in vitro* high-resolution studies monitoring structural dynamics of the cell wall in response to chemical, enzymatic and microbial degradation.

In conclusion, we have applied a multi-platform approach to understanding the detailed high-resolution structural and chemical composition of the plant cell wall in a system that allows the examination of discrete components of xylem tissue. For both basic plant science and biofuel research, this system has advantages in enabling the detailed examination of a single cell type that can be analyzed in large numbers. An especially useful feature brought out by this study is the generation of isolated wall fragments that can be used to examine the internal wall structures of xylem cells. Further studies integrating genetic, biophysical and molecular information either by using enzymatic degradation or additional probes (*e.g.* CBMs or antibodies), along with real time studies of structural changes, will help refine current models and understanding of cell wall architecture.

MATERIALS AND METHODS

Culturing And Isolation Of Tracheary Elements

Zinnia elegans seeds var. Canary Bird (Wetsel Inc., Harrisonburg, VA; purchased from Merrifield Gardens, Merrifield, VA) were sterilized for ~5 min with 10% bleach, rinsed with water and soaked for 1 hr. Seeds were then placed in Seed-Starting soil formula (Burpee, Warminster, PA) in a plant stand at room temperature under 16 hr d⁻¹ fluorescent illumination to allow for germination and growth. After 2 weeks, the first true leaves were harvested and surface sterilized with 1% sodium hypochlorite, 0.01% Triton. Leaves were then macerated and the resulting mesophyll cells were harvested and cultured as previously described (Roberts et al., 1992), except that cells were resuspended at a concentration of 10⁵ cells ml⁻¹ in 6-well plates containing 1 µg ml⁻¹ of 6-benzylaminopurine and 1 µg ml⁻¹ of alpha-naphthaleneacetic acid in S-media.

For separation of TEs, a 9-ml gradient of plant tested 72% Percoll (Sigma-Aldrich, St. Louis, MO) in 0.2 M mannitol was generated by centrifugation at 12,000 rpm for 45 min at 17°C using an angle rotor (Sorvall SS-34; Thermo Fisher Scientific Inc., Waltham, MA). 7- to 10-day old cultures were washed and resuspended in 1-ml 0.2 M mannitol and then overlaid onto the Percoll gradient. After centrifugation using the aforementioned parameters, three distinct bands were removed by gentle aspiration. Percoll fractions of TEs were washed 3 times with ddH₂O before labeling or imaging.

Fluorescence Labeling And Population Analysis

Roughly 3 mg of density-fractionated TEs (wet pellet) were incubated on a Nutator mixer (TCS Scientific Corp., New Hope, PA) with 0.1 µg µl⁻¹ of GFP-tagged CBM3 (Ding et al., 2006) in 150 µl of 1% BSA, PBS buffer (Porter et al., 2007) at room temperature for 1.5 hrs. TEs were then washed 3 times with buffer using a tabletop Nanofuge (Hoefer Scientific Instruments, Holliston, MA) and mounted for fluorescent imaging. Images were acquired using a DMI6000B Leica Microscope equipped with a CCD camera (DFC360FX) and the AF6000 Leica software (JH Technologies Inc., San Jose, CA).

For population analysis of TE fluorescence following CBM3 labeling, images captured using a 20x objective were analyzed using ImageJ (<http://rsb.info.nih.gov/ij/>). Polygons were drawn around isolated TEs and the average fluorescence and area within these polygons were measured. The total fluorescence was calculated by multiplying the average fluorescence by the total number of pixels encompassing each TE. Statistical comparison of the fluorescence values from all populations was performed using the Kruskal-Wallis statistical test.

Sonication and Oxidative Treatment

TEs were broken into fragments using an XL2020 ultrasonic sonicator (Misonix, Farmingdale, NY) equipped with a microtip. Sonication was controlled manually and performed 2 times for 30 s plus one time for 1 min on ice at Level 4.

Intact TEs or fragments were incubated in acidified chlorite (1% sodium chlorite, 0.14% acetic acid) at 70°C for 20 hrs (Leavitt and Danzer, 1993) in a single extraction step. As a control,

incubations were performed in ddH₂O under the same conditions. TEs were then washed 3 times with ddH₂O before additional manipulation.

High-resolution FTIR spectromicroscopy

A high-humidity microscope stage chamber was built to maintain TEs hydrated, overcoming the water interference during high-resolution FTIR spectromicroscopy measurements. All measurements were made in transmission mode and performed with a Nicolet Magna 760 FTIR bench and a Nicolet Nic-Plan IR microscope (Thermo Fisher Scientific Inc., Waltham, MA) equipped with a microscope stage chamber at the infrared beamline of the Advanced Light Source (Lawrence Berkeley National Laboratory, Berkeley, CA, <http://infrared.als.lbl.gov/>). Each spectrum represents an average of 4 scans over a wavenumber range of 4000 to 650 cm⁻¹ at a spectral resolution of 4 cm⁻¹ with an absorption peak position accuracy of 1/100 cm⁻¹. Spectra for at least 10 cells were acquired per condition at a spatial imaging step size of 5 μm. All data processing was performed using Thermo Electron's Omnic 7.2 (<http://www.thermo.com/>) and chemical assignment was carried out as described previously (Delort-Laval et al., 1991). Additional details regarding chemical peak assignment can be found in other recent publications (Kacurakova et al., 2000; Wilson et al., 2000; Carpita et al., 2001). To generate heat maps, in each pixel the absorbance values at the specified wavenumbers were normalized to the maximum value of the absorption at the corresponding wavenumber from the TE incubated in water at 25°C.

Spectral changes associated with TE heterogeneity in wall composition before and after treatments were verified using PCA-LDA. Briefly, it involved two steps. First, spectral data in the fingerprint region (900-1800 cm⁻¹) and in the vibrational region (2750-3700 cm⁻¹) from each pixel inside a TE were extracted and combined to form the original data matrix. In this data matrix preparation, we randomly chose 5 TEs for each condition. PCA was performed using Matlab (The MathWorks Inc., Natick, MA) to calculate the eigenvector and eigenvalue of the covariance matrix of the original data matrix. Then, LDA was performed using the scores of the first five PCA components as property variables, and solving the eigenvector and eigenvalue of the between-class covariance matrix over the within-class covariance matrix. The first two eigenvectors with two highest eigenvalues were chosen as PCA-LD1 and PCA-LD2, and the

projection scores of each sample along these two directions were plotted. The mean and standard deviation for each treatment group were calculated from the PCA-LDA scores plots, and the confidence intervals at $\alpha = 0.05$ around the average scores/individual conditions were estimated and drawn as ellipses. Each data point plotted corresponded to a spectrum acquired from a 5-by-5 μm pixel.

Atomic force microscopy

Droplets of mesophyll cells and density-fractionated TE suspensions in ddH₂O were deposited on plastic coverslips and allowed to air dry. Images were collected using a Nanoscope IV atomic force microscope (Digital Instruments/Veeco, Santa Barbara, CA) operated in tapping mode. For low-resolution analysis and mapping of cell samples, fast scanning AFM probes (DMSAP Micro-Actuated, Veeco Instruments) with a force constant of ~ 1 to 5 N/m and a resonance frequency of ~ 200 kHz were utilized. For high-resolution imaging SuperSharpSilicon (SSS) AFM probes (NanoWorld AG, Neuchâtel, Switzerland) with force constants of ~ 40 N/m and resonance frequencies of ~ 300 kHz were used. The typical radius of SSS AFM tip is ~ 2 nm and the tip height is 10 to 15 μm , which allowed the delineation of high-resolution structural features on relatively rough plant cell surfaces. Tapping amplitude, phase, height and fast-Z (when applicable) images were collected simultaneously. Nanoscope software 5.30r3sr3 was used for acquisition and subsequent processing of AFM images. Size measurements were obtained from at least two images from replicate samples. Height images were contrast-enhanced and, in certain cases, flattened for presentation purposes.

ACKNOWLEDGEMENTS

We thank Dr. Selim Elhadj for assistance with AFM, Dr. Amy Hiddessen for helpful discussions and technical contributions to the project at LLNL, and Dr. Qi Xu at NREL for help with cloning and expression of *CtCBM3-GFP*. We also thank Sabrina Fletcher for her diligent work illustrating the model in Figure 6.

LITERATURE CITED

- Barceló AR** (1995) Peroxidase and not laccase is the enzyme responsible for cell-wall lignification in the secondary thickening of xylem vessels in *Lupinus*. *Protoplasma* **186**: 41-44
- Benova-Kakosova A, Digonnet C, Goubet F, Ranocha P, Jauneau A, Pesquet E, Barbier O, Zhang Z, Capek P, Dupree P, Liskova D, Goffner D** (2006) Galactoglucomannans increase cell population density and alter the protoxylem/metaxylem tracheary element ratio in xylogenetic cultures of *Zinnia*. *Plant Physiol* **142**: 696-709
- Bierhorst DW** (1960) Observations on tracheary elements. *Phytomorphology* **10**: 249-305
- Burgess J, Linstead P** (1984) In-vitro tracheary element formation - structural studies and the effect of tri-iodobenzoic acid. *Planta* **160**: 481-489
- Carpita NC, Defernez M, Findlay K, Wells B, Shoue DA, Catchpole G, Wilson RH, McCann MC** (2001) Cell wall architecture of the elongating maize coleoptile. *Plant Physiol* **127**: 551-565
- Carpita NC, Gibeaut DM** (1993) Structural models of primary cell walls in flowering plants: consistency of molecular structure with the physical properties of the walls during growth. *Plant J* **3**: 1-30
- Chanzy H, Imada K, Mollard A, Vuong R, Barnoud F** (1979) Crystallographic aspects of sub-elementary cellulose fibrils occurring in the wall of rose cells cultured in vitro. *Protoplasma* **100**: 303-316
- Cosgrove DJ** (2005) Growth of the plant cell wall. *Nat Rev Mol Cell Biol* **6**: 850-861
- Crawford SA, Higgins MJ, Mulvaney P, Wetherbee R** (2001) Nanostructure of the diatom frustule as revealed by atomic force and scanning electron microscopy. *J Phycol* **37**: 543-554
- Davies LM, Harris PJ** (2003) Atomic force microscopy of microfibrils in primary cell walls. *Planta* **217**: 283-289
- Delort-Laval J, Bertin C, Robert P, Bertrand D** (1991) Characterization of microbial degradation of plant cell-walls by mid-infrared spectroscopy. *In* GC Galletti, ed, Production and utilization of lignocellulosics: Plant refinery and breeding. Elsevier Applied Science, p 387
- Ding SY, Himmel ME** (2006) The maize primary cell wall microfibril: a new model derived from direct visualization. *J Agric Food Chem* **54**: 597-606
- Ding SY, Xu Q, Ali MK, Baker JO, Bayer EA, Barak Y, Lamed R, Sugiyama J, Rumbles G, Himmel ME** (2006) Versatile derivatives of carbohydrate-binding modules for imaging of complex carbohydrates approaching the molecular level of resolution. *Biotechniques* **41**: 435-442
- Dufrene YF** (2008a) Atomic force microscopy and chemical force microscopy of microbial cells. *Nat Protoc* **3**: 1132-1138
- Dufrene YF** (2008b) Towards nanomicrobiology using atomic force microscopy. *Nat Rev Microbiol* **6**: 674-680
- Fahlen J, Salmen L** (2005) Pore and matrix distribution in the fiber wall revealed by atomic force microscopy and image analysis. *Biomacromolecules* **6**: 433-438
- Falconer MM, Seagull RW** (1988) Xylogenesis in tissue-culture III: continuing wall deposition during tracheary element development. *Protoplasma* **144**: 10-16
- Fantner GE, Barbero RJ, Gray DS, Belcher AM** (2010) Kinetics of antimicrobial peptide activity measured on individual bacterial cells using high-speed atomic force microscopy. *Nat Nanotechnol* **5**: 280-285
- Fujino T, Sone Y, Mitsuishi Y, Itoh T** (2000) Characterization of cross-links between cellulose microfibrils, and their occurrence during elongation growth in pea epicotyl. *Plant Cell Physiol* **41**: 486-494
- Fukuda H** (2004) Signals that control plant vascular cell differentiation. *Nat Rev Mol Cell Biol* **5**: 379-391
- Fukuda H, Komamine A** (1980) Establishment of an experimental system for the study of tracheary element differentiation from single cells isolated from the mesophyll of *Zinnia elegans*. *Plant Physiol* **65**: 57-60

- Fukuda H, Komamine A** (1982) Lignin synthesis and its related enzymes as markers of tracheary-element differentiation in single cells isolated from the mesophyll of *Zinnia elegans*. *Planta* **155**: 423-430
- Green JW** (1963) Wood cellulose. In WR L., ed, *Methods in Carbohydrate Chemistry*, Vol 3. Academic Press, New York, NY
- Hoh JH, Lal R, John SA, Revel JP, Arnsdorf MF** (1991) Atomic force microscopy and dissection of gap junctions. *Science* **253**: 1405-1408
- Ito Y, Ino R, Yoshida S, Fukuda H** (2004) Establishment of a new *Zinnia* experimental system including separation of the distinct cell population with flow cytometry and its culture. *Plant Biotechnol* **21**: 103-108
- Kacurakova M, Capek P, Sasinkova V, Wellner N, Ebringerova A** (2000) FT-IR study of plant cell wall model compounds: pectic polysaccharides and hemicelluloses. *Carbohydr Polym* **43**: 195-203
- Karlsson M, Melzer M, Prokhorenko I, Johansson T, Wingsle G** (2005) Hydrogen peroxide and expression of hIpI-superoxide dismutase are associated with the development of secondary cell walls in *Zinnia elegans*. *J Exp Botany* **56**: 2085-2093
- Kirby AR, Gunning AP, Waldron KW, Morris VJ, Ng A** (1996) Visualization of plant cell walls by atomic force microscopy. *Biophys J* **70**: 1138-1143
- Kodera N, Sakashita M, Ando T** (2006) Dynamic proportional-integral-differential controller for high-speed atomic force microscopy. *Rev Sci Instrum* **77**: 83704-83707
- Kuznetsov Yu G, Malkin AJ, Land TA, DeYoreo JJ, Barba AP, Konnert J, McPherson A** (1997) Molecular resolution imaging of macromolecular crystals by atomic force microscopy. *Biophys J* **72**: 2357-2364
- Leavitt SW, Danzer SR** (1993) Method for batch processing small wood samples to holocellulose for stable-carbon isotope analysis. *Anal Chem* **65**: 87-89
- Lehtio J, Sugiyama J, Gustavsson M, Fransson L, Linder M, Teeri TT** (2003) The binding specificity and affinity determinants of family 1 and family 3 cellulose binding modules. *Proc Natl Acad Sci USA* **100**: 484-489
- Liu YS, Zeng YN, Luo YH, Xu Q, Himmel ME, Smith SJ, Ding SY** (2009) Does the cellulose-binding module move on the cellulose surface? *Cellulose* **16**: 587-597
- Malkin AJ, McPherson A, Gershon PD** (2003) Structure of intracellular mature vaccinia virus visualized by in situ atomic force microscopy. *J Virol* **77**: 6332-6340
- McCann MC, Bush M, Milioni D, Sado P, Stacey NJ, Catchpole G, Defernez M, Carpita NC, Hofte H, Ulvskov P, Wilson RH, Roberts K** (2001) Approaches to understanding the functional architecture of the plant cell wall. *Phytochemistry* **57**: 811-821
- McCann MC, Wells B, Roberts K** (1990) Direct visualization of cross-links in the primary plant-cell wall. *J Cell Sci* **96**: 323-334
- McCartney L, Blake AW, Flint J, Bolam DN, Boraston AB, Gilbert HJ, Knox JP** (2006) Differential recognition of plant cell walls by microbial xylan-specific carbohydrate-binding modules. *Proc Natl Acad Sci USA* **103**: 4765-4770
- McCartney L, Gilbert HJ, Bolam DN, Boraston AB, Knox JP** (2004) Glycoside hydrolase carbohydrate-binding modules as molecular probes for the analysis of plant cell wall polymers. *Anal Biochem* **326**: 49-54
- Mellerowicz EJ, Baucher M, Sundberg B, Boerjan W** (2001) Unravelling cell wall formation in the woody dicot stem. *Plant Mol Biol* **47**: 239-274
- Milioni D, Sado PE, Stacey NJ, Domingo C, Roberts K, McCann MC** (2001) Differential expression of cell-wall-related genes during the formation of tracheary elements in the *Zinnia* mesophyll cell system. *Plant Mol Biol* **47**: 221-238
- Morris VJ, Gunning AP, Kirby AR, Round A, Waldron K, Ng A** (1997) Atomic force microscopy of plant cell walls, plant cell wall polysaccharides and gels. *Int J Biol Macromol* **21**: 61-66

- Muller DJ, Baumeister W, Engel A** (1999) Controlled unzipping of a bacterial surface layer with atomic force microscopy. *Proc Natl Acad Sci USA* **96**: 13170-13174
- Nakashima J, Mizuno T, Takabe K, Fujita M, Saiki H** (1997) Direct visualization of lignifying secondary wall thickenings in *Zinnia elegans* cells in culture. *Plant Cell Physiol* **38**: 818-827
- Pauly M, Keegstra K** (2008) Cell-wall carbohydrates and their modification as a resource for biofuels. *Plant J* **54**: 559-568
- Plomp M, Leighton TJ, Wheeler KE, Hill HD, Malkin AJ** (2007) In vitro high-resolution structural dynamics of single germinating bacterial spores. *Proc Natl Acad Sci USA* **104**: 9644-9649
- Poggi MA, Mancosky DG, Bottomley LA, Lucia LA** (2005) Atomic force microscopic analysis of hydrogen peroxide bleached kraft northern black spruce fibres. *J Microsc-Oxford* **220**: 77-83
- Porter SE, Donohoe BS, Beery KE, Xu Q, Ding SY, Vinzant TB, Abbas CA, Himmel ME** (2007) Microscopic analysis of corn fiber using starch- and cellulose-specific molecular probes. *Biotechnol Bioeng* **98**: 123-131
- Roberts AW, Haigler CH** (1994) Cell expansion and tracheary element differentiation are regulated by extracellular pH in mesophyll cultures of *Zinnia elegans* L. *Plant Physiol* **105**: 699-706
- Roberts AW, Koonce LT, Haigler CH** (1992) A simplified medium for *in vitro* tracheary element differentiation in mesophyll suspension-cultures from *Zinnia elegans* L. *Plant Cell Tiss Org* **28**: 27-35
- Roberts K, McCann MC** (2000) Xylogenesis: the birth of a corpse. *Curr Opin Plant Biol* **3**: 517-522
- Roland JC, Vian B, Reis D** (1975) Observations with cytochemistry and ultracytometry on fine-structure of expanding walls in actively elongating plant-cells. *J Cell Sci* **19**: 239-259
- Salnikov VV, Grimson MJ, Delmer DP, Haigler CH** (2001) Sucrose synthase localizes to cellulose synthesis sites in tracheary elements. *Phytochemistry* **57**: 823-833
- Scheuring S, Dufrene YF** (2010) Atomic force microscopy: probing the spatial organization, interactions and elasticity of microbial cell envelopes at molecular resolution. *Mol Microbiol* **75**: 1327-1336
- Simola J, Malkavaara P, Alen R, Peltonen J** (2000) Scanning probe microscopy of pine and birch kraft pulp fibres. *Polymer* **41**: 2121-2126
- Somerville C, Bauer S, Brininstool G, Facette M, Hamann T, Milne J, Osborne E, Paredes A, Persson S, Raab T, Vorwerk S, Youngs H** (2004) Toward a systems approach to understanding plant cell walls. *Science* **306**: 2206-2211
- Stacey NJ, Roberts K, Carpita NC, Wells B, McCann MC** (1995) Dynamic changes in cell surface molecules are very early events in the differentiation of mesophyll cells from *Zinnia elegans* into tracheary elements. *Plant J* **8**: 891-906
- Taylor JG, Owen TP, Koonce LT, Haigler CH** (1992) Dispersed lignin in tracheary elements treated with cellulose synthesis inhibitors provides evidence that molecules of the secondary cell-wall mediate wall patterning. *Plant J* **2**: 959-970
- Thelen MP, Northcote DH** (1989) Identification and purification of a nuclease from *Zinnia elegans* L - a potential molecular marker for xylogenesis. *Planta* **179**: 181-195
- Thimm JC, Burritt DJ, Ducker WA, Melton LD** (2000) Celery (*Apium graveolens* L.) parenchyma cell walls examined by atomic force microscopy: effect of dehydration on cellulose microfibrils. *Planta* **212**: 25-32
- Tormo J, Lamed R, Chirino AJ, Morag E, Bayer EA, Shoham Y, Steitz TA** (1996) Crystal structure of a bacterial family-III cellulose-binding domain: a general mechanism for attachment to cellulose. *EMBO J* **15**: 5739-5751
- Touhami A, Jericho MH, Beveridge TJ** (2004) Atomic force microscopy of cell growth and division in *Staphylococcus aureus*. *J Bacteriol* **186**: 3286-3295
- Turner S, Gallois P, Brown D** (2007) Tracheary element differentiation. *Ann Rev Plant Biol* **58**: 407-433

- Twumasi P, Schel JH, van Ieperen W, Woltering E, Van Kooten O, Emons AM** (2009) Establishing *in vitro* *Zinnia elegans* cell suspension culture with high tracheary element differentiation. *Cell Biol Int* **33**: 524-533
- Viani MB, Pietrasanta LI, Thompson JB, Chand A, Gebeshuber IC, Kindt JH, Richter M, Hansma HG, Hansma PK** (2000) Probing protein-protein interactions in real time. *Nat Struct Biol* **7**: 644-647
- Vorwerk S, Somerville S, Somerville C** (2004) The role of plant cell wall polysaccharide composition in disease resistance. *Trends Plant Sci* **9**: 203-209
- Wilson RH, Smith AC, Kacurakova M, Saunders PK, Wellner N, Waldron KW** (2000) The mechanical properties and molecular dynamics of plant cell wall polysaccharides studied by Fourier-transform infrared spectroscopy. *Plant Physiol* **124**: 397-405
- Weir IE, Maddumage R, Allan AC, Ferguson IB** (2005) Flow cytometric analysis of tracheary element differentiation in *Zinnia elegans* cells. *Cytometry A* **68**: 81-91
- Xu Q, Tucker MP, Arenkiel P, Ai X, Rumbles G, Sugiyama J, Himmel ME, Ding SY** (2009) Labeling the planar face of crystalline cellulose using quantum dots directed by type-I carbohydrate-binding modules. *Cellulose* **16**: 19-26
- Yan L, Li W, Yang J, Zhu Q** (2004) Direct visualization of straw cell walls by AFM. *Macromol Biosci* **4**: 112-118
- Zimmermann T, Thommen V, Reimann P, Hug HJ** (2006) Ultrastructural appearance of embedded and polished wood cell walls as revealed by Atomic Force Microscopy. *J Struct Biol* **156**: 363-369

FIGURE LEGENDS

Figure 1. Separation of differentiated tracheary elements from mesophyll cells. A and B, Brightfield (left) and fluorescence (right) image pairs are shown. Autofluorescence (450 to 490 nm), which mainly originates from lignin in secondary wall thickenings in TEs, is shown. A, Transdifferentiation of cultured *Zinnia elegans* mesophyll cells into TEs results in a combination of TEs, mesophyll, and dead cells. The inset shows the detail of a mature TE of ~50 μm in length with a secondary wall patterned in a mostly reticulate network. B, Separation using density gradient centrifugation generates fractions highly enriched in TEs. C and E, Brightfield images. D and F, AFM images; fast Z for (D) and amplitude for (F). For AFM, cells were dried on the substrate and thus appear flattened with their contents bulging out. C and D, Mesophyll cells possess chloroplasts and other organelles evident by both by light microscopy and AFM. Arrowheads point to the location of chloroplasts (D). E and F, Tracheary elements can be distinguished by the presence of prominent secondary wall thickenings, which are arranged in spiral in the particular example shown. Arrowheads point to the location of secondary cell wall thickenings (F).

Figure 2. CBM3 labeling of tracheary elements after oxidative treatment. A to D, Representative brightfield and fluorescence image pairs are shown. A and B, TEs incubated in water at 70°C for 20 hrs; C and D, TEs incubated in 1% sodium chlorite, 0.14% acetic acid at 70°C for 20 hrs. A and C, unlabeled TEs; B and D, TEs labeled with *Ct*CBM3-GFP, a fluorescently labeled family 3 carbohydrate-binding module that binds to cellulose. A, Unlabeled TEs exhibit a low level of autofluorescence between 512 and 542 nm after incubation in water at 70°C. For presentation purposes, all fluorescent images were scaled consistently so that this panel had a low, yet noticeable signal level. B, TEs incubated in water are, on average, ~5-fold more fluorescent after labeling with *Ct*CBM3-GFP. C, TEs treated with acidified chlorite show a dramatic loss of autofluorescence. D, TEs treated with acidified chlorite and labeled with *Ct*CBM3-GFP have the highest fluorescence of all the samples analyzed. E, The total fluorescence of single TEs is plotted on a log scale as a function of area. For each population, at least 35 TEs were analyzed. The fluorescence of unlabeled TEs after acidified chlorite treatment (open circles) is comparable to background levels. The largest increase in fluorescence (on average, ~1000-fold) is evident in the population of TEs treated with acidified

chlorite and labeled with *CtCBM3*-GFP (closed circles). When compared by Kruskal-Wallis test, all populations are significantly different ($p < 0.0001$).

Figure 3. The topography of TE cell walls revealed by atomic force microscopy. Contrast-enhanced AFM height images are shown. A and B, Representative images of the surface of TEs incubated in water at 70°C for 20 hrs show a fairly uniform outer layer of granular material. B, Zoomed image corresponding to the box in (A) displays granules ranging in size between ~20 and 50 nm. Some fibers can be observed embedded within this granular matrix (arrowheads). C to F, Images of TEs after incubation with acidified chlorite at 70°C for 20 hrs. C and D, In most cases, the surfaces of TEs appear stripped of the granular matrix observed in TEs incubated in water (A, B), and a meshwork of fibrils is exposed. D, Zoomed image corresponding to the box in (C) shows fibrils. Cellulose fibrils range in width between ~8 and 15 nm. E and F, In some cases, the granular matrix covering the surface of TEs is partially resistant to removal by acidified chlorite treatment. E, The underlying meshwork of fibrils is evident through a hole in the outermost granular layer. F, Clumps of granules can also appear embedded within fibrils. Some fibrils appear to run over and through these granular clumps (arrowhead).

Figure 4. Chemical composition of TEs characterized by high-resolution synchrotron radiation-based infrared spectromicroscopy. A to C, Brightfield images (leftmost) and pseudocolored heat maps (right) corresponding to absorbances at the specified wavenumbers from representative TEs are shown. Brightfield images were acquired through an infrared objective. Heat maps are normalized to the maximum absorbance of a TE incubated in water at 25°C for 20 hrs (A) at the corresponding wavenumber; red corresponds to a ratio of 1.0, while blue corresponds to 0 (see heat scale bar). A, TEs incubated in water at 25°C show a considerable amount of signal intensity from general cell wall components, and more specifically from cellulosic, hemicellulosic, and pectic materials. A large amount of lignin is also evident as a high signal at ~1510 cm^{-1} . B, Incubation in water at 70°C for 20 hrs results in the loss of some signal at ~1738 cm^{-1} and ~1040 cm^{-1} , which correspond to hemicellulosic and pectic material. C, Incubation in acidified chlorite at 70°C for 20 hrs results in dramatic loss of signal from lignin at ~1510 cm^{-1} . Hemicellulosic and pectic materials also appear to be lost after this treatment. D, Average absorbance values plotted for 5 randomly chosen TEs are shown for the conditions in (A) in

green, (B) in blue, and (C) in red. Wavenumbers corresponding to the chemical components shown in (A-C) are labeled. The broad peak near 3400 cm^{-1} mostly corresponds to hydroxyl groups in the cell wall as well as water inside the TEs. E, Principal Component Analysis and Linear Discriminant Analysis (PCA-LDA) were performed on the infrared spectra from the same 5 randomly chosen TEs. PC scores along the first two modes of variation are plotted for each condition. Confidence intervals at $\alpha = 0.05$ for all three populations are drawn as ellipses. PCA-LDA separates the population of TEs treated with acidified chlorite from the TEs incubated in water at 25°C or 70°C based on their infrared spectral signatures.

Figure 5. TE fragments reveal secondary wall structure. A and B, Brightfield images; C, DIC image. A, An overview of TEs after mild sonication is shown. Different types of TEs fragments as well as seemingly intact TEs were observed. B, Ring-like structures (arrow) and spirals (arrowhead) from secondary wall thickenings, as well as smaller fragments and cell debris (two arrowheads), are shown following density separation by centrifugation. C, Fragments from reticulate secondary wall networks were also observed. D to F, AFM images of a secondary wall ring (D) and a reticulate network (E, F) are labeled with regions corresponding to the numbered zoomed images. AFM height images were contrast-enhanced for presentation. D, The secondary wall ring shown represents a transverse cross-section of a TE. An outermost layer of granular material covers the secondary wall thickening. Regions 1 to 5 depict primarily cellulose fibrils that are arranged in parallel and concentrically, and a granular matrix within the ring. In some cases, the observed granules appear to be aggregated into larger structures (region 1) and some fibers appear to run across the main orientation of the cellulose fibrils (region 4 and 5). E and F, Images correspond to a secondary wall fragment of a reticulate network similar to that shown in (C). Acidified chlorite treatment removes the granular material and reveals that fibrils are arranged mostly parallel to the length of thickenings. Some debris, which did not affect imaging, is apparent (E). Several fibrils appear to run across the main orientation of the cellulose fibrils (region 6). F, Fibrils change orientation in large groups at intersecting points on a secondary wall network. Fibrils can also become bundled to form thicker cellulose structures (arrowhead).

Figure 6. Model of the cell wall architecture of a single *Zinnia elegans* tracheary element. The three main layers of the cell wall observed are depicted: (1) an outermost granular matrix

enveloping the TE, (2) the primary cell wall composed of cellulose microfibrils organized in a meshwork, and (3) the inner secondary cell wall thickenings containing mainly cellulose microfibrils arranged in a parallel orientation. Cellulose microfibrils within the native cell wall are embedded within a granular matrix, which is not depicted for presentation purposes. The cellulose microfibrils and outermost granular layer are not shown to scale.

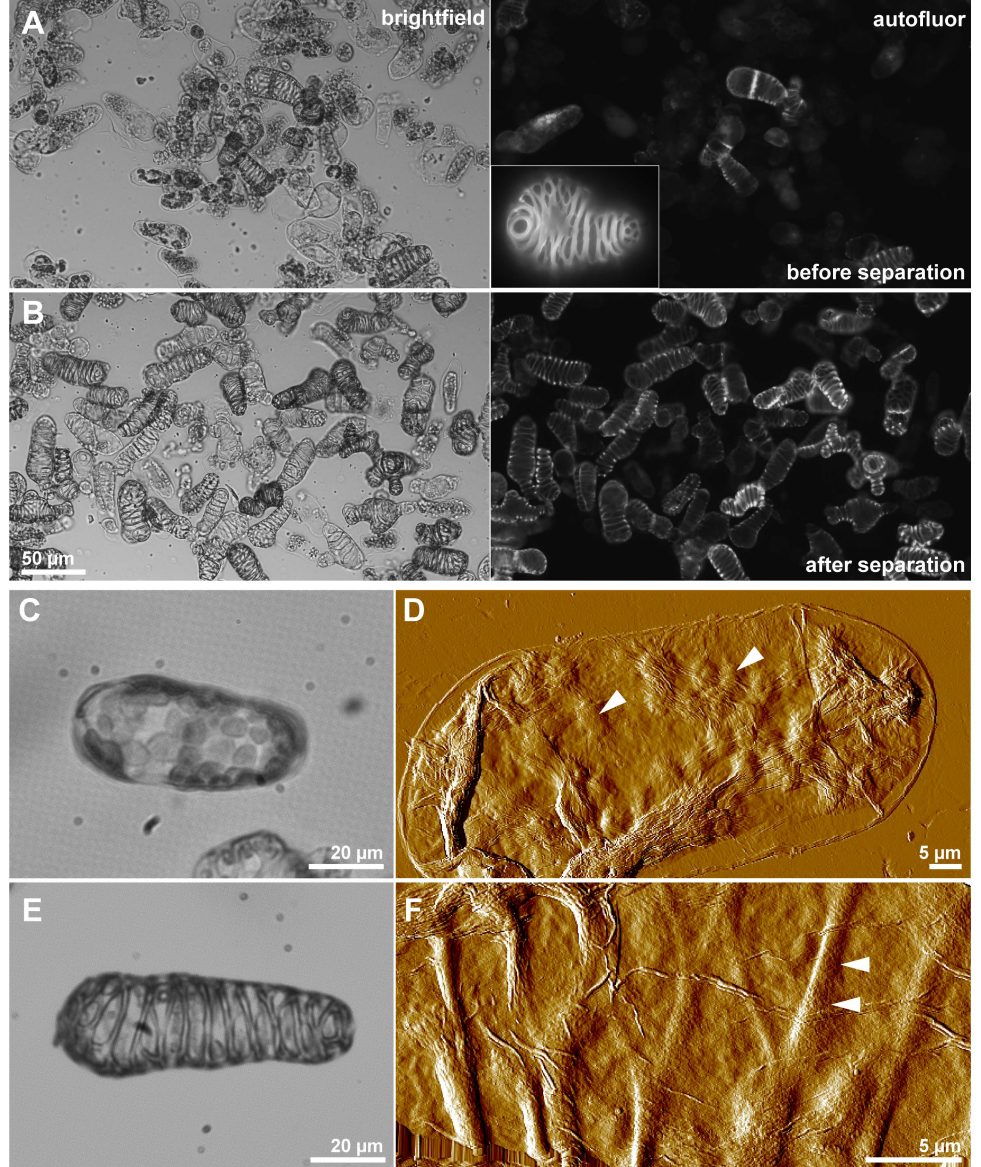


Figure 1. Separation of differentiated tracheary elements from mesophyll cells. A and B, Brightfield (left) and fluorescence (right) image pairs are shown. Autofluorescence (450 to 490 nm), which mainly originates from lignin in secondary wall thickenings in TEs, is shown. A, Transdifferentiation of cultured *Zinnia elegans* mesophyll cells into TEs results in a combination of TEs, mesophyll, and dead cells. The inset shows the detail of a mature TE of ~50 μm in length with a secondary wall patterned in a mostly reticulate network. B, Separation using density gradient centrifugation generates fractions highly enriched in TEs. C and E, Brightfield images. D and F, AFM images; fast Z for (D) and amplitude for (F). For AFM, cells were dried on the substrate and thus appear flattened with their contents bulging out. C and D, Mesophyll cells possess chloroplasts and other organelles evident by both by light microscopy and AFM. Arrowheads point to the location of chloroplasts (D). E and F, Tracheary elements can be distinguished by the presence of prominent secondary wall thickenings, which are arranged in spiral in the particular example shown. Arrowheads point to the location of secondary cell wall thickenings (F).

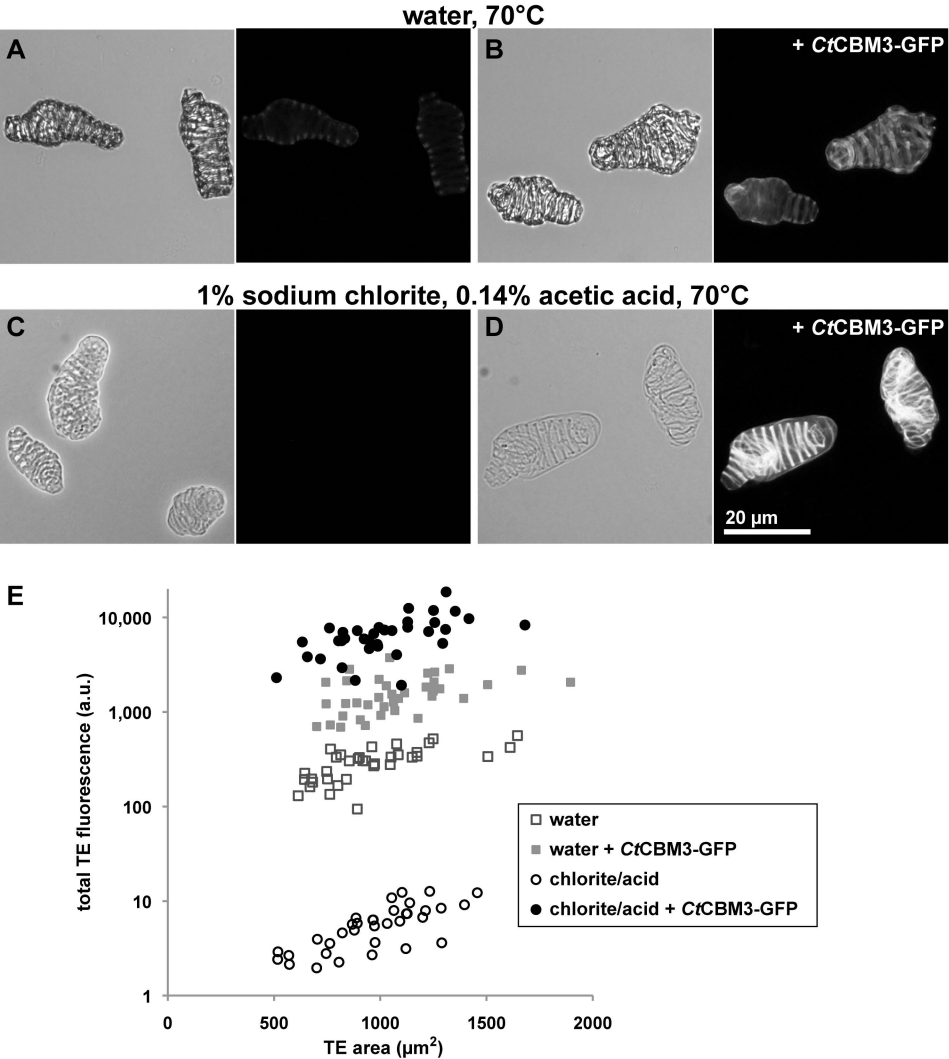
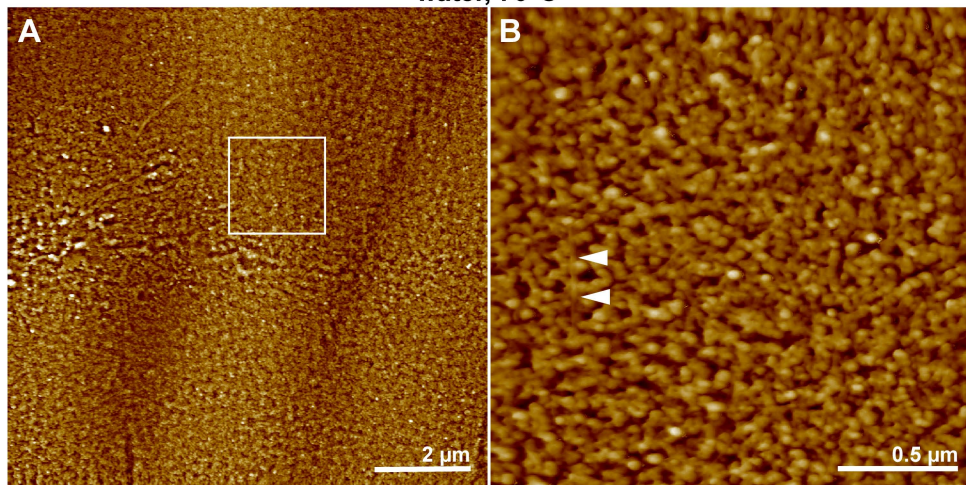


Figure 2. CBM3 labeling of tracheary elements after oxidative treatment. A to D, Representative brightfield and fluorescence image pairs are shown. A and B, TEs incubated in water at 70°C for 20 hrs; C and D, TEs incubated in 1% sodium chlorite, 0.14% acetic acid at 70°C for 20 hrs. A and C, unlabeled TEs; B and D, TEs labeled with CtCBM3-GFP, a fluorescently labeled family 3 carbohydrate-binding module that binds to cellulose. A, Unlabeled TEs exhibit a low level of autofluorescence between 512 and 542 nm after incubation in water at 70°C. For presentation purposes, all fluorescent images were scaled consistently so that this panel had a low, yet noticeable signal level. B, TEs incubated in water are, on average, ~5-fold more fluorescent after labeling with CtCBM3-GFP. C, TEs treated with acidified chlorite show a dramatic loss of autofluorescence. D, TEs treated with acidified chlorite and labeled with CtCBM3-GFP have the highest fluorescence of all the samples analyzed. E, The total fluorescence of single TEs is plotted on a log scale as a function of area. For each population, at least 35 TEs were analyzed. The fluorescence of unlabeled TEs after acidified chlorite treatment (open circles) is comparable to background levels. The largest increase in fluorescence (on average, ~1000-fold) is evident in the population of TEs treated with acidified chlorite and labeled with CtCBM3-GFP (closed circles). When compared by Kruskal-Wallis test, all populations are significantly different ($p < 0.0001$).

water, 70°C



1% sodium chlorite, 0.14% acetic acid, 70°C

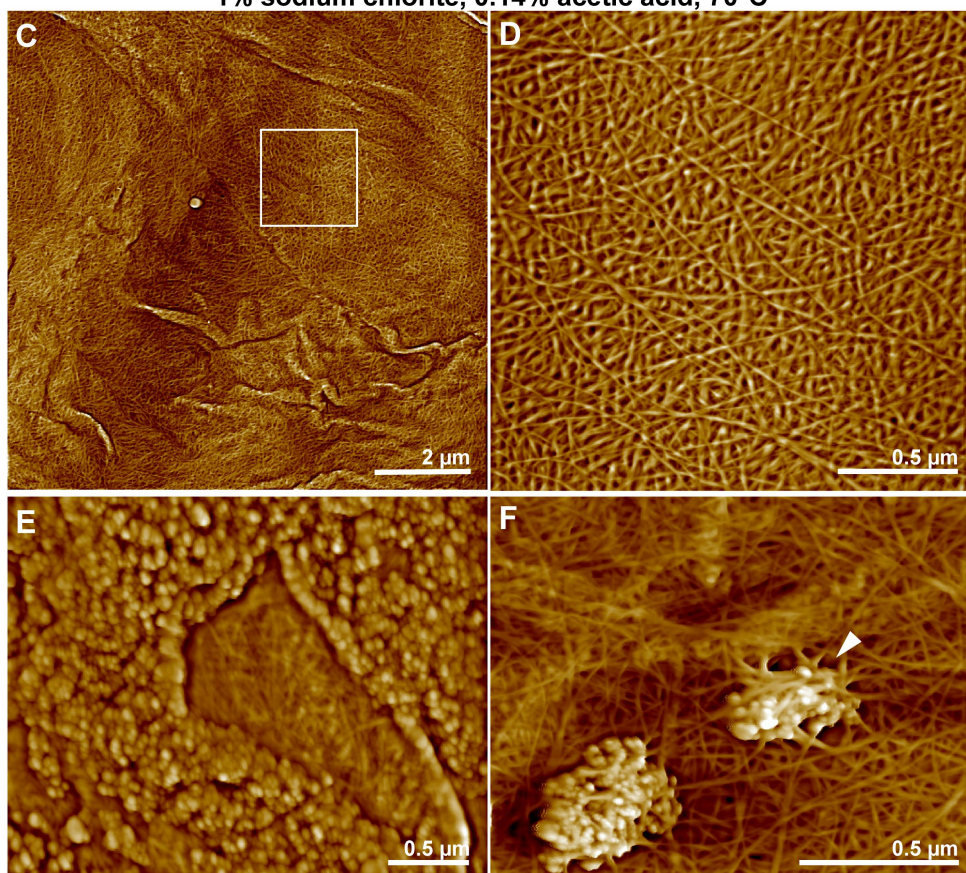


Figure 3. The topography of TE cell walls revealed by atomic force microscopy. Contrast-enhanced AFM height images are shown. A and B, Representative images of the surface of TEs incubated in water at 70°C for 20 hrs show a fairly uniform outer layer of granular material. B, Zoomed image corresponding to the box in (A) displays granules ranging in size between ~20 and 50 nm. Some fibers can be observed embedded within this granular matrix (arrowheads). C to F, Images of TEs after incubation with acidified chlorite at 70°C for 20 hrs. C and D, In most cases, the surfaces of TEs appear stripped of the granular matrix observed in TEs incubated in water (A, B), and a meshwork of fibrils is exposed. D, Zoomed image corresponding to the box in (C) shows fibrils. Cellulose fibrils range in width between ~8 and 15 nm. E and F, In some cases, the granular matrix covering the surface of TEs is partially resistant to removal by acidified chlorite treatment. E, The underlying meshwork of fibrils is evident through a hole in the outermost granular layer. F, Clumps of granules can also appear embedded within fibrils. Some fibrils appear to run over and through these granular clumps (arrowhead).

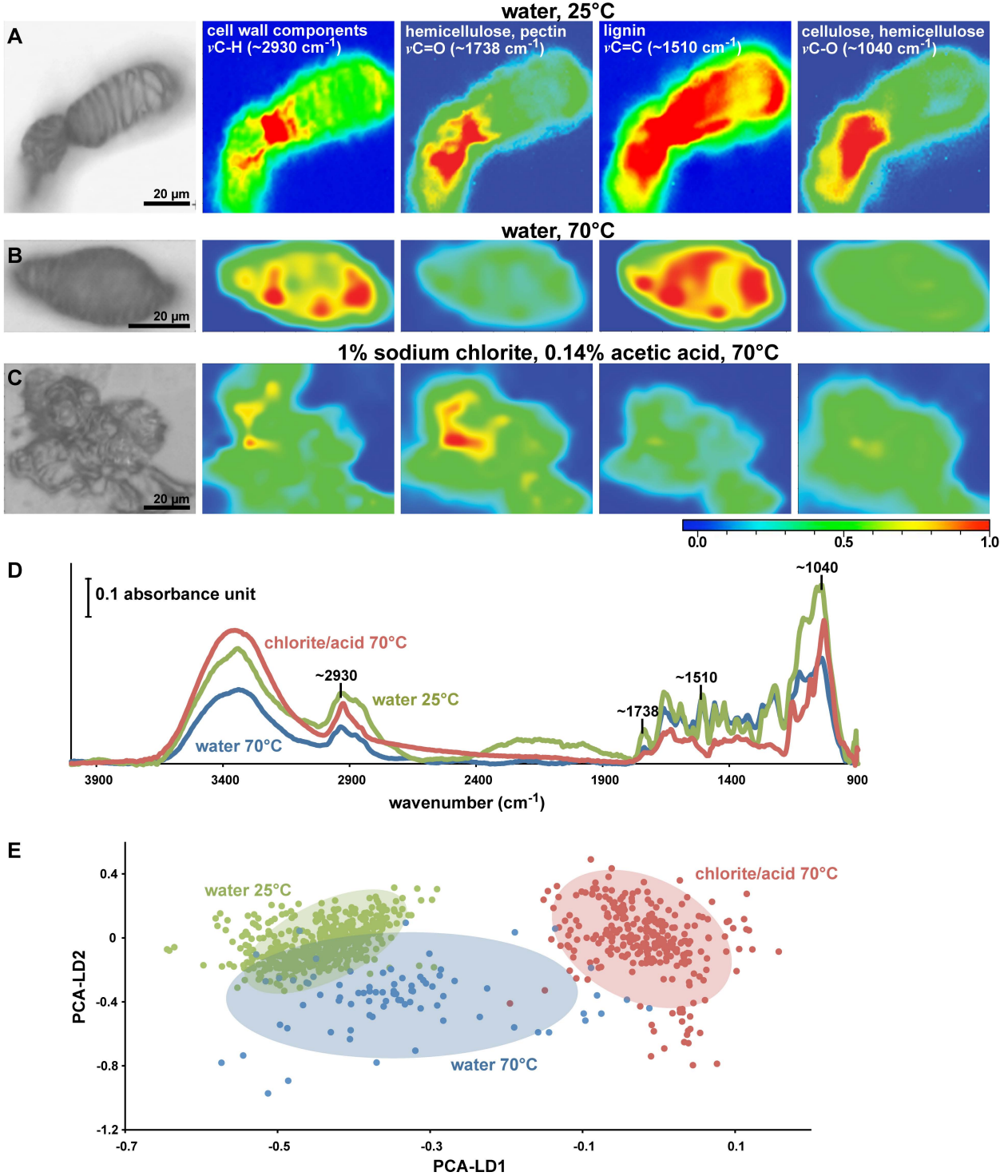


Figure 4. Chemical composition of TEs characterized by high-resolution synchrotron radiation-based infrared spectromicroscopy. A to C, Brightfield images (leftmost) and pseudocolored heat maps (right) corresponding to absorbances at the specified wavenumbers from representative TEs are shown. Brightfield images were acquired through an infrared objective. Heat maps are normalized to the maximum absorbance of a TE incubated in water at 25°C for 20 hrs (A) at the corresponding wavenumber; red corresponds to a ratio of 1.0, while blue corresponds to 0 (see heat scale bar). A, TEs incubated in water at 25°C show a considerable amount of signal intensity from general cell wall components, and more specifically from cellulosic, hemicellulosic, and pectic materials. A large amount of lignin is also evident as a high signal at $\sim 1510\text{ cm}^{-1}$. B, Incubation in water at 70°C for 20 hrs results in the loss of some signal at $\sim 1738\text{ cm}^{-1}$ and $\sim 1040\text{ cm}^{-1}$, which correspond to hemicellulosic and pectic material. C, Incubation in acidified chlorite at 70°C for 20 hrs results in dramatic loss of signal from lignin at $\sim 1510\text{ cm}^{-1}$. Hemicellulosic and pectic materials also appear to be lost after this treatment. D, Average absorbance values plotted for 5 randomly chosen TEs are shown for the conditions in (A) in green, (B) in blue, and (C) in red. Wavenumbers corresponding to the chemical components shown in (A-C) are labeled. The broad peak near 3400 cm^{-1} mostly corresponds to hydroxyl groups in the cell wall as well as water inside the TEs. E, Principal Component Analysis and Linear Discriminant Analysis (PCA-LDA) were performed on the infrared spectra from the same 5 randomly chosen TEs. PC scores along the first two modes of variation are plotted for each condition. Confidence intervals at $\alpha = 0.05$ for all three populations are drawn as ellipses. PCA-LDA separates the population of TEs treated with acidified chlorite from the TEs incubated in water at 25°C or 70°C based on their infrared spectral signatures.

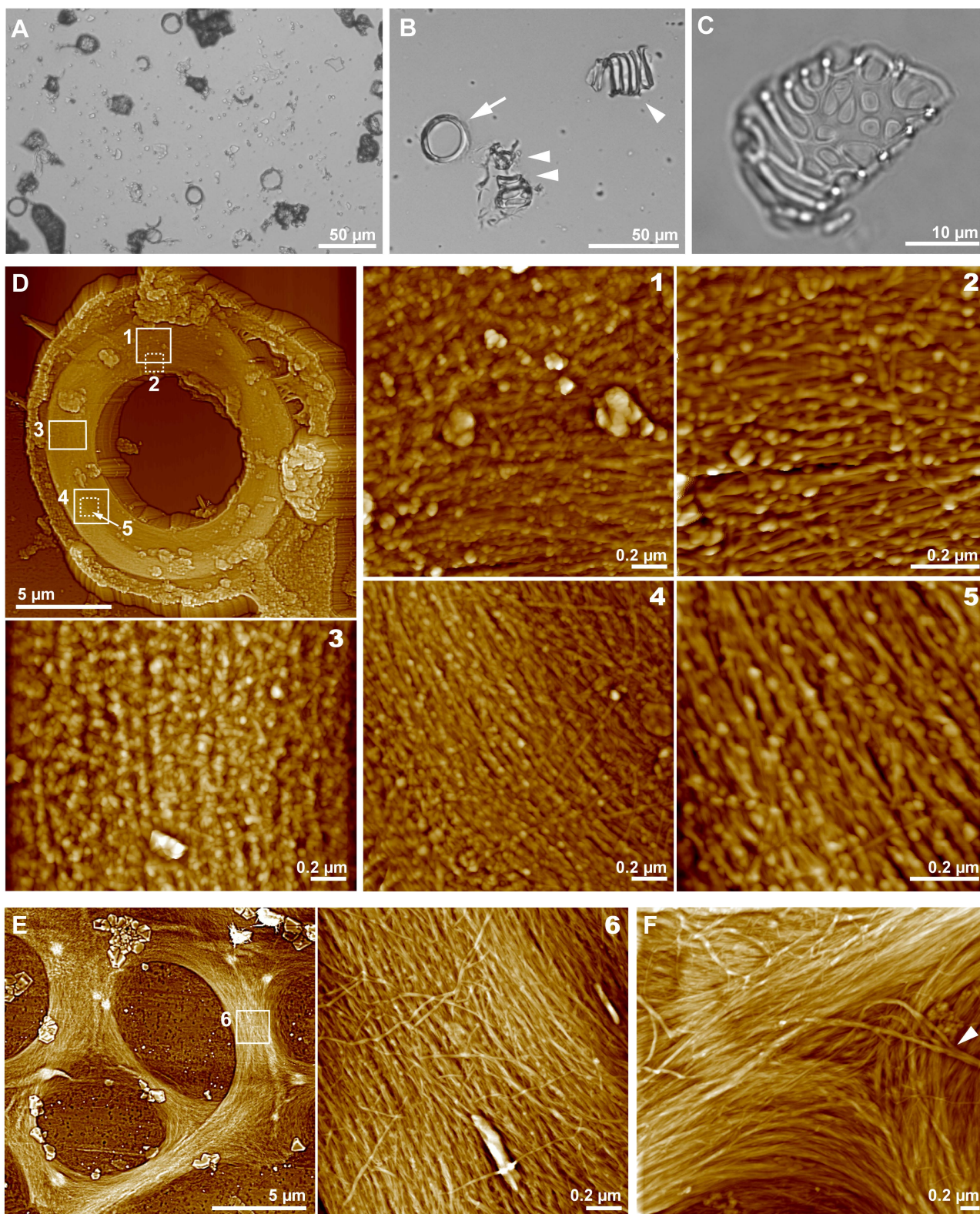


Figure 5. TE fragments reveal secondary wall structure. A and B, Brightfield images; C, DIC image. A, An overview of TEs after mild sonication is shown. Different types of TEs fragments as well as seemingly intact TEs were observed. B, Ring-like structures (arrow) and spirals (arrowhead) from secondary wall thickenings, as well as smaller fragments and cell debris (two arrowheads), are shown following density separation by centrifugation. C, Fragments from reticulate secondary wall networks were also observed. D to F, AFM images of a secondary wall ring (D) and a reticulate network (E, F) are labeled with regions corresponding to the numbered zoomed images. AFM height images were contrast-enhanced for presentation. D, The secondary wall ring shown represents a transverse cross-section of a TE. An outermost layer of granular material covers the secondary wall thickening. Regions 1 to 5 depict primarily cellulose fibrils that are arranged in parallel and concentrically, and a granular matrix within the ring. In some cases, the observed granules appear to be aggregated into larger structures (region 1) and some fibers appear to run across the main orientation of the cellulose fibrils (region 4 and 5). E and F, Images correspond to a secondary wall fragment of a reticulate network similar to that shown in (C). Acidified chlorite treatment removes the granular material and reveals that fibrils are arranged mostly parallel to the length of thickenings. Some debris, which did not affect imaging, is apparent (E). Several fibrils appear to run across the main orientation of the cellulose fibrils (region 6). F, Fibrils change orientation in large groups at intersecting points on a secondary wall network. Fibrils can also become bundled to form thicker cellulose structures (arrowhead).

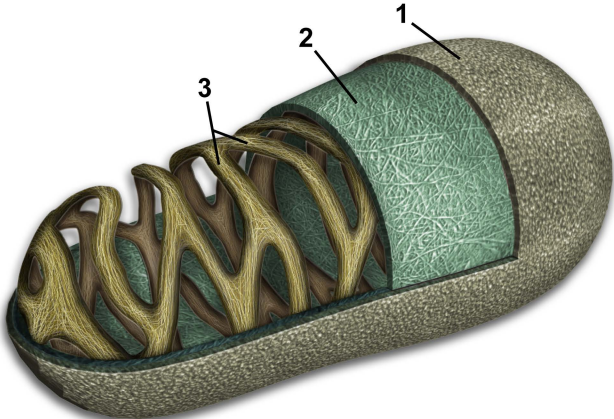


Figure 6. Model of the cell wall architecture of a single *Zinnia elegans* tracheary element. The three main layers of the cell wall observed are depicted: (1) an outermost granular matrix enveloping the TE, (2) the primary cell wall composed of cellulose microfibrils organized in a meshwork, and (3) the inner secondary cell wall thickenings containing mainly cellulose microfibrils arranged in a parallel orientation. Cellulose microfibrils within the native cell wall are embedded within a granular matrix, which is not depicted for presentation purposes. The cellulose microfibrils and outermost granular layer are not shown to scale.